Article

Numerical Modelling of the Hydrodynamic Performance of Biodegradable Drifting Fish Aggregating Devices in Currents

Tongzheng Zhang [1], Junbo Zhang [2], Qinglian Hou [2], Gangyi Yu [2], Ao Chen [2], Zhiqiang Liu [2,*] and Rong Wan [1,*]

[1]   National Engineering Research Center for Oceanic Fisheries, Key Laboratory of Sustainable Exploitation of Oceanic Fisheries Resources, College of Marine Living Resource Sciences and Management, Shanghai Ocean University, Shanghai 201306, China; zhangtongzheng7@163.com

[2]   College of Marine Living Resource Sciences and Management, Shanghai Ocean University, Shanghai 201306, China

*   Correspondence: lzhiqiang716@126.com (Z.L.); rongwan@shou.edu.cn (R.W.)

Abstract: Fish Aggregating Devices (FADs) are essential supplementary structures used in tropical tuna purse-seine fishing. They are strategically placed to attract tuna species and enhance fishing productivity. The hydrodynamic performance of FADs has a direct effect on their structural and environmental safety in the harsh marine environment. Conventional FADs are composed of materials that do not break down naturally, leading to the accumulation of waste in the ocean and potential negative effects on marine ecosystems. Therefore, this work aimed to examine the hydrodynamic performance of biodegradable drifting FADs (Bio-DFADs) in oceanic currents by numerical modelling. The Reynolds-averaged Navier–Stokes equation was used to solve the flow field and discretized based on the realizable k-ε turbulence model, employing the finite volume method. A set of Bio-DFADs was developed to assess the hydrodynamic performance under varying current velocities and attack angles, as well as different balsa wood diameters and sinker weights. The results indicated that the relative current velocity significantly affected the relative velocity of Bio-DFADs. The relative length of the raft significantly affected both the relative velocity and the relative wetted area in a pure stream. Finally, the diameter of the balsa wood affected the drift velocity, and the sinker's relative weight affected the hydrodynamic performance of the Bio-DFADs.

Keywords: biodegradable drifting Fish Aggregating Devices (Bio-DFADs); hydrodynamic performance; fluid–structure interaction; current

1. Introduction

Approximately 66% of the worldwide tuna harvest is obtained by tuna purse-seine vessels, with 36% originating from sets of drifting Fish Aggregating Devices (DFADs) in tropical tuna fisheries [1]. Tropical tuna purse-seine vessels operate in the equatorial waters of the pelagic oceans. They use a large number of DFADs to gather tuna species and improve their fishing efficiency. It is estimated that over 100,000 DFADs are deployed annually by these vessels. Numerous studies have examined this practice [2–9]. However, the majority of traditional DFADs consist of synthetic and non-biodegradable netting materials, which contribute to marine litter, the entanglement of sensitive species, and other negative impacts on the ecosystem. These consequences have been documented in various studies [10–17]. Most DFADs endure a lengthy amount duration underwater in the ocean and are subjected to a range of oceanographic conditions, such as currents, waves, and biofouling. The proliferation of DFADs in the open ocean is an issue, considering their adverse effects on the marine environment. Research on the hydrodynamic performance of DFADs helps elucidate the structural features that are well-suited for maritime environments. Additionally, different materials possess distinct fracture strengths that significantly influence the safety of structures. The hydrodynamic performance of the Bio-DFADs in

oceanic currents is also crucial for identifying the overall drifting characteristics, functioning as free-drifting marine infrastructure. Consequently, it is essential to focus on the hydrodynamic performance and material concerns in practical conditions to successfully apply DFADs.

Extensive studies have been conducted to examine the numerical methodology for analyzing stiff and flexible bodies [18–25]. In recent decades, several investigators have studied the hydrodynamic performance of DFADs. Investigating the hydrodynamic performance of DFADs is necessary to improve the safety and efficiency of fish aggregation [26,27]. To enhance the environmental safety of DFADs in marine environments, a variety of DFADs have been constructed using biodegradable materials. These materials were employed to investigate the impact of various structural characteristics on wave conditions through experimental tests and numerical simulations [18,26]. In addition to waves, the current is an essential factor in the design of marine infrastructure. Lee et al. (2018) [28] deployed the particle image velocimetry method to analyze the velocity and turbulence intensity of high-risk net-type and low-risk rope-type DFADs in multiple current conditions. The results showed a notable difference in the drift velocity of the low-risk rope-type DFADs.

However, prior research has concentrated on the motion responses of DFADs in marine waves. The hydrodynamic characteristics of the Bio-DFADs in the presence of a current have not been fully investigated. Notably, Bio-DFADs comprise a combination of a small-scale raft and a flexible structure. The flexible structure of the Bio-DFADs, especially when submerged, is often exposed to fluid currents. Moreover, biofouling has an impact on the hydrodynamic properties of biodegradable rafts and ropes, which impairs their structural integrity. Determining the drift velocity of Bio-DFADs in various currents aids in clarifying the optimal deployment strategy. Hence, it is necessary to investigate the hydrodynamic properties of Bio-DFADs in flowing currents.

This study presents a numerical modelling scheme that evaluates the interaction between current and Bio-DFADs in three dimensions. The Bio-DFADs contained biodegradable materials, such as bamboo and cotton rope, making them environmentally acceptable for the marine ecosystem. Herein, STAR-CCM+ software 14.02 was used to compute the hydrodynamic performance of the Bio-DFADs under various current conditions. We adopted the finite volume method to discretize the Reynold-averaged Naviers–Stokes equations (RANS). The Euler overlay method was used to reduce the level of reflection at the boundaries. Finally, the motion responses of the Bio-DFADs in current were derived by employing the dynamic fluid–body interaction (DFBI) model.

2. Materials and Methods

2.1. Description of the Bio-DFADs

This study aimed to perform numerical simulations of Bio-DFADs in the presence of steady currents. Figure 1 depicts a schematic representation of the Bio-DFADs, and Table 1 lists the major properties of the Bio-DFADs. The Bio-DFAD model comprises three components: raft, rope, and sinker. The raft is composed of two perpendicular layers of equidistant balsa wood sticks. The balsa wood raft eventually degrades, which is beneficial when the Bio-DFADs are lost or abandoned. This type of raft has been employed for constructing the Bio-DFADs in the actual ocean [16]. A total of five buoys, which are agreed to be used in the design of DFADs, are attached to the top part of the raft. The buoys, made of Ethylene Vinyl Acetate Copolymer (EVA) material, provide buoyancy to the overall structure. Each float is shaped like an ellipsoidal sphere, with a length of 24 cm and both width and height of 12 cm. The rope is fastened to the bottom section of the raft at one end, and on the other end, it is linked to a steel sinker weighing 2.00, 4.00, 6.00, 8.00, 10.00, 12.00, and 14.00 kg.
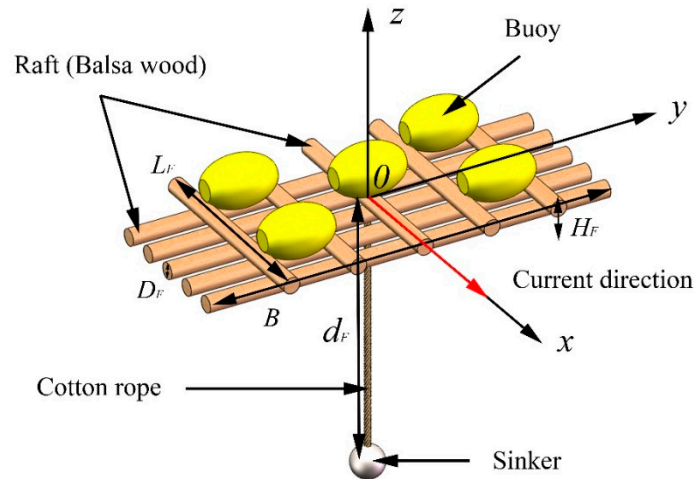
Figure 1. A schematic of the Bio-DFAD model.

Table 1. The main characteristics of the Bio-DFAD model.

Main Characteristics	Parameter	Value
Length of the raft	L_F	0.50, 1.00, 1.50 m
Width of the raft	B	1.00 m
Height of the raft	H_F	0.06, 0.08, 0.10, 0.12, 0.14, 0.16 m
Diameter of the balsa wood stick	D_F	0.03, 0.04, 0.05, 0.06, 0.07, 0.08 m
Length of the rope	d_F	0.60 m
Weight of the sinker	W_{Sinker}	2.00, 4.00, 6.00, 8.00, 10.00, 12.00, 14.00 kg

2.2. Test Conditions

The Bio-DFADs were subjected to heave, pitch, and surge motions in pure currents during the numerical simulations. We investigated a total of ten current speed cases based on monitoring data from the tuna purse-seine fleets. The current velocity, U, was specified as 0.10, 0.20, 0.30, 0.40, 0.50, 0.60, 0.70, 0.80, 0.90, and 1.00 m/s. Various attack angles, denoted as α, were also examined, as depicted in Figure 2. The test conditions are presented in Table 2. The computational fluid dynamics (CFD) simulations of Bio-DFADs in currents were initially conducted in tranquil water circumstances, followed by the consideration of 10 different current regimes. The 10 current speeds were derived based on the concept of a flat wave in volume of fluid (VOF) wave models.
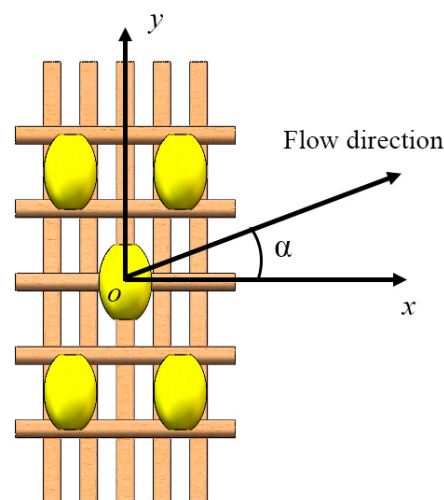
Figure 2. The attack angle between the Bio-DFADs and flow direction.

Table 2. Test conditions of the Bio-DFAD simulations.

Cases	Current Velocity U (m/s)	Attack Angle α (°)
Calm water	0.10, 0.20, 0.30, 0.40, 0.50, 0.60, 0.70, 0.80, 0.90, 1.00	0, 90

2.3. Numerical Setup

2.3.1. Governing Equations and Turbulence Model

Reynolds-averaged Navier–Stokes (RANS) simulations using the realizable k-ε turbulence model with two-layer all y+ wall treatment are adopted in the present study [29]. The realizable k-ε model is considered to be more effective than other turbulence models in accurately estimating the distribution of the dissipation rate [30]. The RANS method is a feasible and widely acknowledged solution for turbulence modelling and can provide a rational prediction for turbulent flows from ocean structures. The mass and momentum conservation equations are solved using CFD software (STAR-CCM+) and the overset mesh method. For incompressible flows, the averaged continuity and momentum equations can be expressed as follows:

$$\frac{\partial \rho}{\partial t} + \frac{\partial (\rho u_i)}{\partial x_i} = 0 \tag{1}$$

$$\frac{\partial (\rho u_i)}{\partial t} + \frac{\partial (\rho u_i u_j)}{\partial x_j} = -\frac{\partial P}{\partial x_i} + \rho g_i + \frac{\partial}{\partial x_j}\left[\mu\left(\frac{\partial u_i}{\partial x_j} + \frac{\partial u_j}{\partial x_i}\right) - \overline{u_i' u_j'}\right] \tag{2}$$

where t represents the time, ρ represents the fluid density, P represents the mean pressure, S represents the closed surface, U_i represents the average velocity (i, j = 1, 2, 3 represent the x, y, and z directions in the Cartesian coordinate system), g_i represents the gravitational acceleration, μ represent the dynamic viscosity of the fluid, u_i, and u_j denote the mean velocities in directions i and j, respectively, u_i' and u_j' denote the turbulence velocities in directions i and j, respectively, and $-\overline{u_i' u_j'}$ denote the Reynolds stress.

Typically, the RANS equations are solved using the finite volume method. The governing equations are discretized using second-order schemes in space and second-order implicit schemes in time. The VOF approach is used to accurately distinguish between the two phases (i.e., air and water phases) of the free surface (Hirt and Nichols, 1981) [31]. The convective term in the VOF transport equations is discretized using the high-resolution interface capturing approach proposed by Hirt and Nichols in 1981 [31]. The turbulence modelling is based on a realizable k-ε model with a two-layer all y+ wall treatment. The equations for the transmission of turbulent kinetic energy, k, and the specific dissipation rate of turbulence, ε, are the following:

k equation

$$\frac{\partial (\rho k)}{\partial t} + \frac{\partial (\rho k u_i)}{\partial x_i} = \frac{\partial}{\partial x_j}\left[\left(\mu + \frac{\mu_t}{\sigma_k}\right)\frac{\partial k}{\partial x_j}\right] + G_k - \rho\varepsilon \tag{3}$$

ε equation

$$\frac{\partial (\rho \varepsilon)}{\partial t} + \frac{\partial (\rho \varepsilon u_i)}{\partial x_i} = \frac{\partial}{\partial x_j}\left[\left(\mu + \frac{\mu_t}{\sigma_\varepsilon}\right)\frac{\partial \varepsilon}{\partial x_j}\right] + C_{1\varepsilon}\frac{\varepsilon}{k}G_k - C_{2\varepsilon}\rho\frac{\varepsilon^2}{k} \tag{4}$$

where G_k represents the turbulent kinetic energy generated by the mean velocity gradient, σ_k and σ_ε denote constants representing the turbulent Prandtl numbers, and C_μ, $C_{1\varepsilon}$, and $C_{2\varepsilon}$ denote constants. The model constants for the realizable k-ε turbulence model denote C_μ = 0.09, $C_{1\varepsilon}$ = 1.44, $C_{2\varepsilon}$ = 1.92, σ_k = 1.0, and σ_ε = 1.3 [32,33].

2.3.2. Computational Domain and Boundary Conditions

Figure 3 depicts the computational domain and boundary conditions of the scaled Bio-DFAD model, which was constructed using the Cartesian coordinate system. The coordinate system is center at a position that is $4 L_F$ from the inlet boundary and $10 L_F$ from the outlet boundary. For the width of the computational domain, to reduce the computational cost, the symmetry boundary is set at the place of half width, 3 B from the side boundary. The water depth, denoted by h, is 0.80 m. The coordinate system of the initial position of the Bio-DFAD aligns with the computational domain. Two overlapping sections were used in the computational domain. The overset method is employed to capture the motion responses of the Bio-DFADs. The velocity inlet condition was imposed on the inlet, top, and bottom limits of the domain, with the stated velocity of the flat VOF wave. A pressure outlet condition was imposed on the outlet boundary of the domain, specifying the pressure as the hydrostatic pressure of the flat VOF wave. In addition, the front and rear limits were established as symmetry conditions. To decrease the computational workload, just half of the Bio-DFADs model was used, with the surfaces designated as non-slip wall conditions.
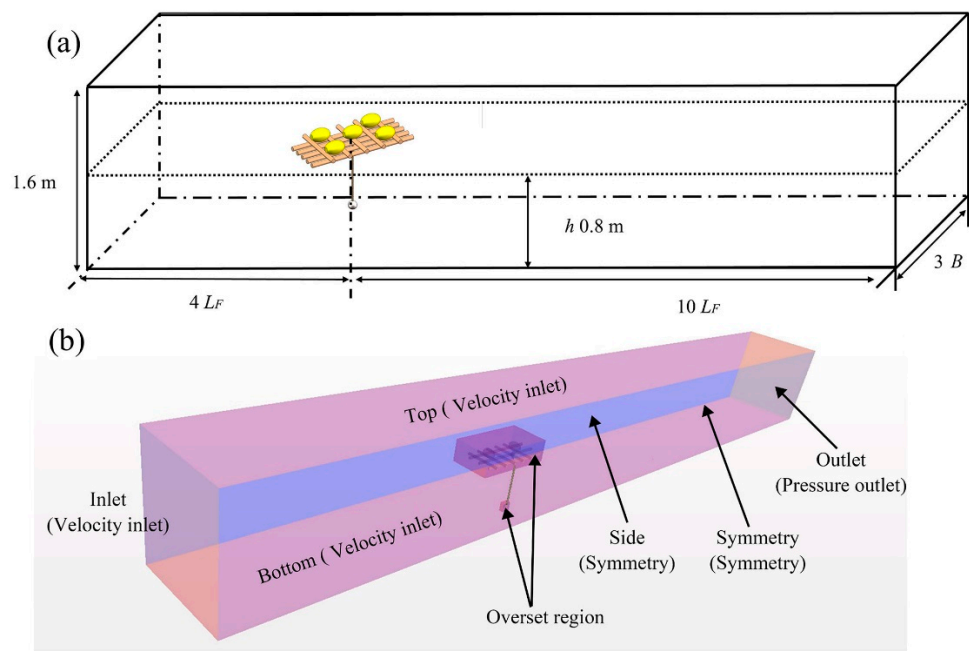
Figure 3. Computational domain and boundary conditions with the scaled Bio-DFADs model: (**a**) the global 3D computational domain; (**b**) boundary conditions.

This research primarily focuses on numerical simulations of the Bio-DFAD's hydrodynamic performance. Owing to its low cost and short duration, CFD simulations are extensively employed in researching the hydrodynamic performance of oceanic structures. The CFD numerical software STAR-CCM+ is used to examine the hydrodynamic properties of the Bio-DFADs and investigate their drift velocity under varying current velocities. The VOF method and six degrees of freedom (6-DOF) solver were used to analyze the hydrodynamic performance of the Bio-DFADs, specifically, the surge, pitch, and heave motions of the Bio-DFADs. The 6-DOF solver modified the position and orientation of the DFAD body. The DFBI model was used to simulate the movements of the Bio-DFADs in reaction to pressure and shear forces inside the flow domain, as well as the force exerted by the catenary. In the DFBI model, the RANS solver was used to compute the dynamic forces and moments exerted on the Bio-DFADs and adjust the position of the rigid body. The rope in the Bio-DFADs system was represented by a catenary in the body couplings of the STAR-CCM+ package, as illustrated in Figure 3b. The catenary coupling model was used to simulate the elastic, quasi-stationary rope that hangs between two endpoints, namely the

raft and sinker, and is affected by its own weight in the gravitational field. The parametric equations that describe the shape of the catenary in the Cartesian coordinate system of the computational domain are expressed as follows (STAR-CCM+, 2019) [34]:

$$x = au + b\sin(u) + \alpha \tag{5}$$

$$y = a\cosh(u) + \frac{b}{2}\sinh^2(u) + \beta \tag{6}$$

$$for \ u_1 \leq u \leq u_2 \tag{7}$$

$$a = \frac{c}{\lambda_0 g} \tag{8}$$

$$b = \frac{ca}{DL_{eq}} \tag{9}$$

$$c = \frac{\lambda_0 L_{eq} g}{\sinh(u_2) - \sinh(u_1)} \tag{10}$$

where g is the value of gravitational acceleration, D represents the stiffness of the catenary, and λ_0 and L_{eq} represent the mass per unit length and relaxation length of the catenary, respectively. The integration constants α and β depend on the position of the two endpoints and the total mass of the catenary. The positions of the two endpoints in the parameter space of the catenary are denoted by u_1 and u_2. The curve parameter, denoted as u, is directly linked to the inclination angle Φ of the catenary curve:

$$\tan\Phi = \sinh(u) \tag{11}$$

To enhance the efficiency of the simulations and reduce computational time, the CFD simulation employs the VOF wave-damping approach, as proposed by Choi and Yoon in 2009 [35]. In addition, the VOF wave-damping function was implemented at the outlet border to attenuate the vertical disturbances that propagate towards it and reduce the wave reflections at the boundaries. The wave-damping zone at the outlet side of the computational domain has a length of $2\,L_F$. An additional factor representing resistance is incorporated into the momentum equation for the w-velocity, as described by Gu et al. (2018) [36].

$$S_z^d = \rho(f_1 + f_2|w|)\frac{e^k - 1}{e^1 - 1}w \tag{12}$$

$$k = \left(\frac{x - x_{sd}}{x_{ed} - x_{sd}}\right)^{n_d} \tag{13}$$

where ω represents the vertical velocity component, and f_1, f_2, and n_d are parameters of the damping model. Furthermore, x_{sd} and x_{ed} indicate the start and end locations of the wave-damping zone, respectively.

2.3.3. Motion Equation of the Bio-DFADs

The Bio-DFADs in this study exhibit unrestricted movement in the current, including heave, pitch, and surge motions. The equations of motion for the Bio-DFADs can be represented as the following:

Translation equation

$$m\frac{dv}{dt} = f \tag{14}$$

Rotation equation

$$M\frac{d\omega}{dt} + \omega \times M\omega = n \tag{15}$$

where m represents the mass of the body, f represents the resultant force acting on the body, and v represents the velocity of the centre of mass. The tensor M represents the moment of

inertia, ω represents the angular velocity of the rigid body, and n represents the resultant moment acting on the body, which encompasses the pressure moment, shear moment, and external moment induced by the catenary.

The tensor of the moments of inertia, moment and resultant force acting on the body can be written as:

$$M = \begin{pmatrix} M_{xx} & M_{xy} & M_{xz} \\ M_{xy} & M_{yy} & M_{yz} \\ M_{xz} & M_{yz} & M_{zz} \end{pmatrix} \tag{16}$$

$$n = f_r\left(n_p + n_\tau + \sum n_{ext}\right) \tag{17}$$

$$f = f_r\left(F_p + F_\tau + F_g + \sum F_{ext}\right) \tag{18}$$

The tensor M is symmetric, it can be defined by two vectors: one specifying the principal components, (M_{xx}, M_{yy}, M_{zz}) along the diagonal, and another specifying the off-diagonal components, (M_{xy}, M_{xz}, M_{yz}). F_{ext} and n_{ext} represent the extra forces and moments, F_g is the gravity force, F_p and n_p are the fluid pressure force and moment acting on the body, F_τ and n_τ are the fluid shear force and moment acting on the body, and f_r is the time-ramping function. In this study, there are no extra force and moments forcing the model to move.

2.3.4. Mesh Resolution

The trimmed cell mesher, prism layer mesher, and surface remesher were used to discretize the computational domain. These meshing techniques are well-suited for the intricate geometric characteristics of the Bio-DFAD system. Given that the primary focus of the numerical simulation was the surfaces of the Bio-DFAD model and the surrounding regions, special treatment was applied to the meshes on these surfaces. Ultimately, the appropriate mesh size was determined using a mesh optimization test to ensure the stability and convergence of the simulation. The objective indices chosen for the test were the drift velocity (V), time step, and maximum mesh size. Velocity monitoring at various distances ($D = 1.00$, 2.00, and 3.00 m) from the inflow border (with a current velocity of $U = 0.10$ m/s) was undertaken individually. The calculation achieved stability when the time step and maximum size in the computational domain were set to 0.005 s and 0.64 m, respectively, as demonstrated in Figure 4.
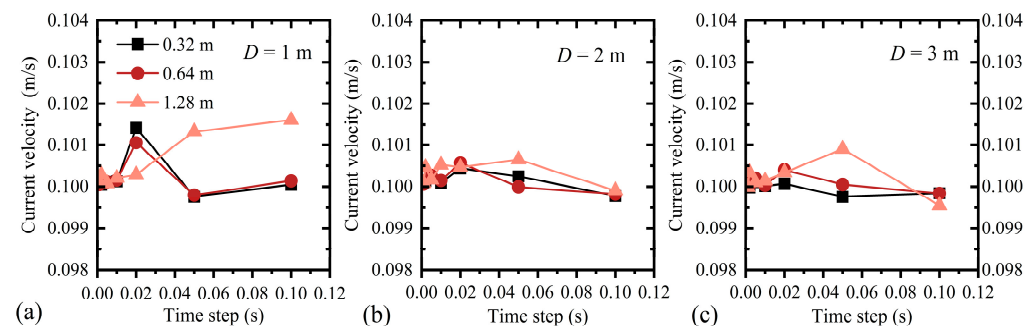
Figure 4. Mesh optimization test with various distances from the inflow border. (**a**) D = 1.00 m, (**b**) D = 2.00 m, (**c**) D = 3.00 m.

Figure 5 shows the current velocity values between numeric and theory calculations. One of the current velocities, 0.50 m/s was selected as the test condition. The monitor point was set at the 1.00 m away from the inlet boundary. Based on the numeric model, the error rate is 0.72%. The results demonstrate that the numerical model established in this study has a high degree of accuracy.
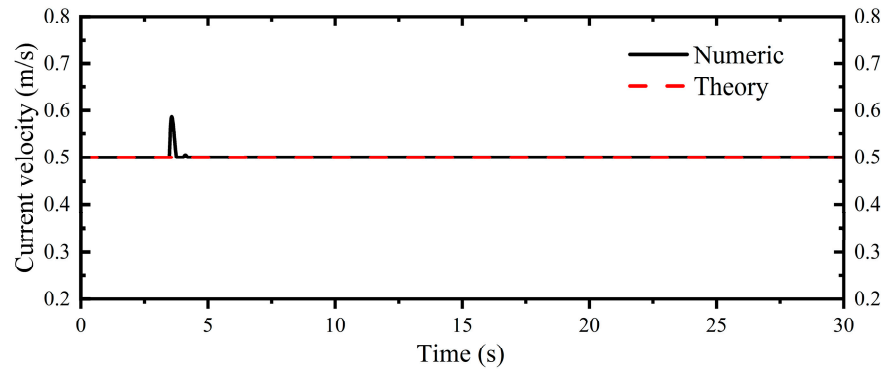
Figure 5. The comparison of current velocity between numeric and theory (0.50 m/s).

Figure 6 depicts the mesh generated in the computational domain. To enhance the precision of the Bio-DFAD responses in currents, two overset mesh zones are used for the raft and sinker. Figure 6 reveals that the meshes in close proximity to the water's surface are more detailed, and the overset meshes near the Bio-DFAD are precisely suited to the body. This allows for accurate simulation of the Bio-DFAD motion responses. To analyze the fluid dynamics surrounding the Bio-DFADs, the thickness of the prism layer is defined as 0.01 m, consisting of five layers. Additionally, a prism layer stretching factor of 1.2 is applied to the wall limits of the Bio-DFADs. The y+ values vary from 30 to 100. The trimmer mesh is employed to incorporate the Bio-DFAD characteristics and discretize the remaining portion of the computational domain. The mesh size scale, represented by the $\Delta x / \Delta z$ ratio, varies between 4 and 1. Specifically, it is equal to 1 in the two overset mesh sections and 4 in the water-free surface. The time-step interval is defined as 0.005 s. To mitigate the numerical dispersion error [32], the Courant number of the VOF model is adjusted to be less than 0.3. Moreover, mesh refinements are employed to accurately capture the surface waves and decrease the number of cells in the computational domain.
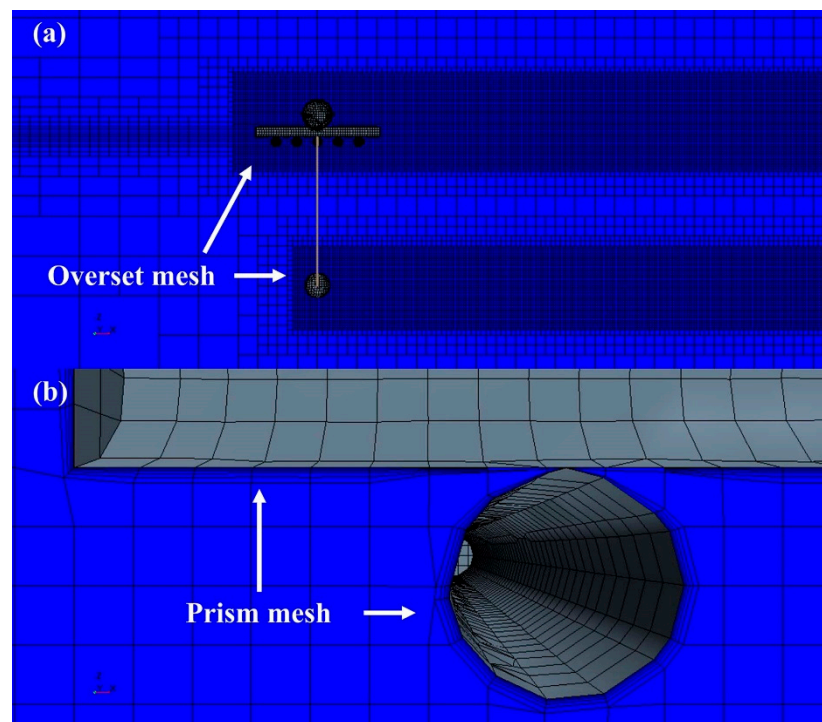
Figure 6. Mesh generation in the computational domain. (**a**) Overset mesh, (**b**) Prism mesh.

3. Results and Discussions

3.1. Effect of the Relative Current Velocity on the Bio-DFADs

Figures 7–9 show the volume of fraction, free surface elevation, and velocity contours of the Bio-DFADs at U = 0.10 m/s, including the top view, side view, and drift velocity contours at different times when the Bio-DFAD motion became relatively stable under a fixed current velocity.
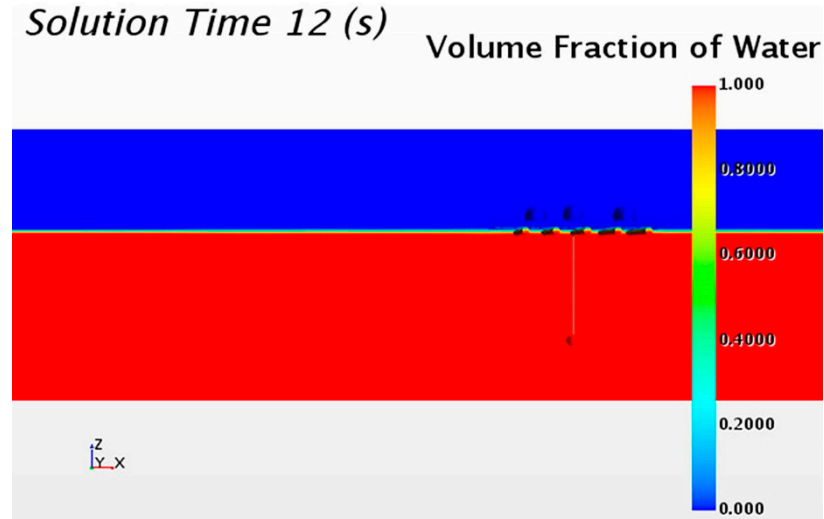
Figure 7. Front view of the volume fraction of water contours of the Bio-DFADs (U = 0.10 m/s).
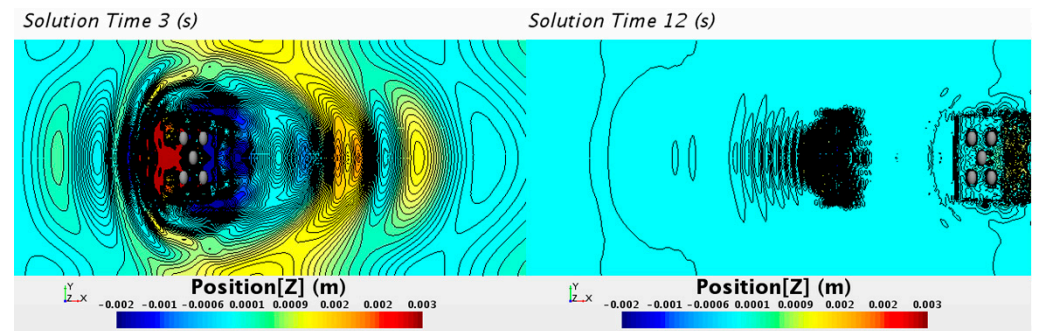
Figure 8. Top view of the free surface elevation contours of the Bio-DFADs (U = 0.10 m/s).
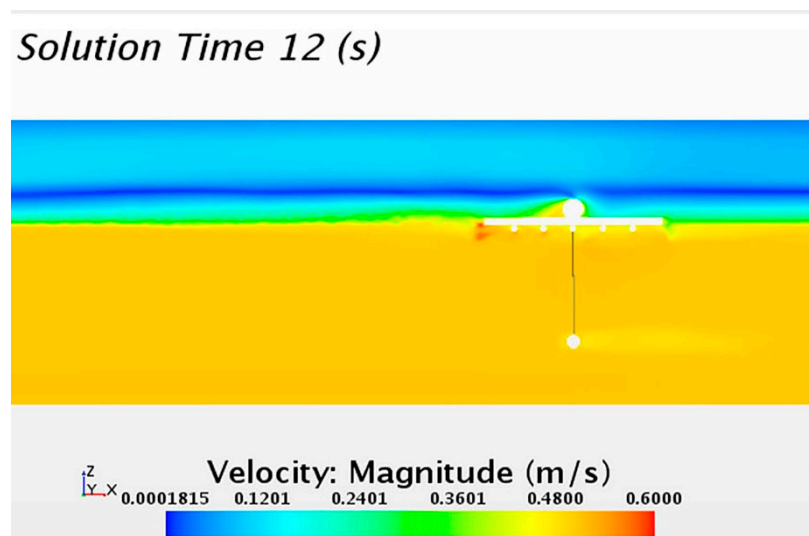
Figure 9. Velocity contours of the Bio-DFADs (U = 0.10 m/s).

To test whether current velocity shows generally distinct activity in response to different hydrodynamic performances, the effects of different current velocities (U) on the drift velocity (V) and the effects of relative current velocities (U/B) on relative velocity (V/U) of the Bio-DFADs were investigated (Figure 10), for $D_F = 40$ mm, $W_{Sinker} = 2.00$ kg, and $\alpha = 0°$. Bio-DFADs with three raft lengths (0.50, 1.00, and 1.50 m) were employed in this study. The drift velocity is calculated through the distance drift per unit time ($\Delta d/\Delta t$) in the current direction. The wetted area is calculated by the area covered by the water to the total area of the raft (S_{Wetted}/S_{Total}), and to indicate the invisibility of the FADs, which is often broken and stolen by other fleets of fishers. As depicted in Figure 10a, the Bio-DFADs exhibited a substantial rise in drift velocity, V, when the current velocity, U, increased. The drift velocity of the model with a balsa wood length of 0.50 m was lower than that of the other two models when the current velocity value was lower. Nevertheless, the disparity in drift velocity among the three models diminished as the current velocity increased. Furthermore, when the current velocity exceeded 0.90 m/s, the drift velocity of the model with a balsa wood length of 0.50 m became slightly greater than the drift velocities of the other two models. Figure 10b depicts the correlation between the relative current velocity, U/B, and the relative velocity, V/U. Initially, the relative velocity of the model with a length of 0.50 m was considerably lower than that of the other two models. The relative velocity had a direct correlation with the balsa wood length, gradually increasing until reaching saturation. The disparity between the 0.50 and 1.00 m models was greater than that between the 1.50 and 1.00 m models. Nevertheless, the disparity diminished as the relative current velocity increased. When the relative current velocity exceeded 0.9, the model with a length of 0.50 m exhibited a somewhat greater relative velocity compared with the other two models. The findings indicated that the relative current velocity had a substantial impact on the relative velocity, and the disparity in relative velocity across the three models tended to be low. The length of the balsa wood also had a significant impact on the relative velocity, although this influence diminished as the relative current velocity increased.
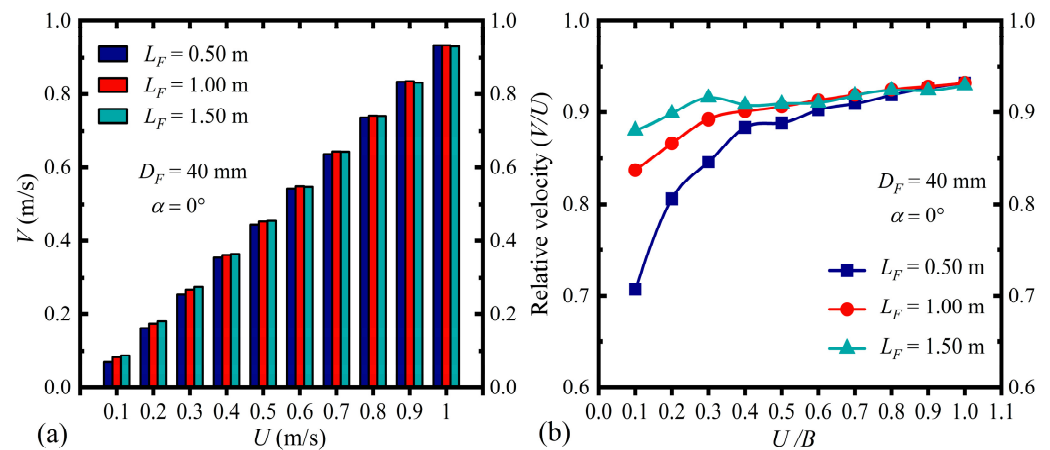
Figure 10. The (**a**) effects of different current velocities (U) on the drift velocity (V) and (**b**) effects of relative current velocities (U/B) on the relative velocity (V/U) of the Bio-DFADs.

The proportion of the wetted area (S_{Wetted}/S_{Total}) for the three models remained stable as the relative current velocity increased. The disparity between the 0.50 and 1.00 m models was greater than that between the 1.00 and 1.50 m models. The wetted area decreased with the increasing length, and the effect diminished as the length increased. A higher wetted area relative to the surroundings suggests a higher level of invisibility. The rope tension slightly increased as the current velocity increased. Additionally, the tension increased as the balsa wood length increased. The findings demonstrated that the relative current velocity had little impact on the relative wetted area and rope tension, but the length affected both the relative wetted area and the relative rope tension.

3.2. Effect of the Relative Length and Attack Angle on the Bio-DFADs

As previously mentioned, the length of Bio-DFADs had a significant effect on relative wetted area and rope tension. The relationships for relative velocity (V/U), relative wetted area (S_{Wetted}/S_{Total}), and relative rope tension (F/W_{Sinker}) with different relative lengths (0.50/1.00, 1.00/1.00, 1.50/1.00, 1.00/0.50, 1.00/1.00, and 1.00/1.50) and attack angles (0°, 90°) are shown in Figure 11. As seen in Figure 11, changes in the relative length and attack angle resulted in changes to the hydrodynamic performance of Bio-DFADs, for D_F = 40 mm, W_{Sinker} = 2.00 kg, and U = 0.50 m/s.
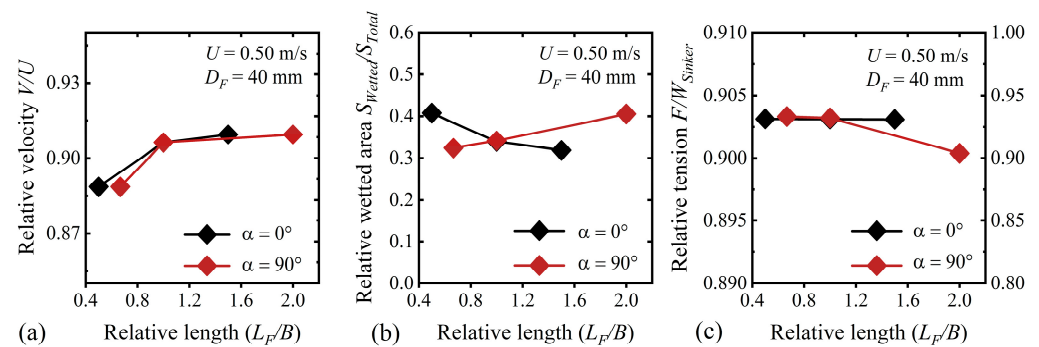
Figure 11. The change in (**a**) relative velocity (V/B), (**b**) wetted area (S_{Wetted}/S_{Total}), and (**c**) rope tension (F/W_{Sinker}) of the Bio-DFADs for different relative lengths and attack angles.

Figure 11a shows the effects of the relative length and attack angle on the relative velocity. The relative velocity was minimized for $\alpha = 0°$, compared with $\alpha = 90°$. When $\alpha = 0°$, the relative velocity increased and then decreased as the relative length increased. When $\alpha = 90°$, the relative velocity increased as the relative length increased. The values at points three and four indeed do not show significant differences. These two points represent the results at different attack angles for a model with an aspect ratio of 1:1. Since most of the raft is submerged in the water, the pressure and drag forces experienced by the model do not differ significantly, leading to negligible differences in relative velocity. As shown in Figure 11b, for $\alpha = 90°$, the relative wetted area was significantly larger than that when $\alpha = 0°$. Additionally, for $\alpha = 0°$, the relative wetted area decreased and then increased as the relative length increased, and the opposite trend was observed for $\alpha = 90°$. As depicted in Figure 11c, as the relative length increased, the relative tension did not change. The relative tension was slightly less for $\alpha = 90°$ than for $\alpha = 0°$. The results indicate that relative length had a significant effect on the relative velocity and relative wetted area under pure current but had almost no influence on the relative tension. Moreover, the attack angle had almost no influence on the hydrodynamic performance of the model. The relative velocity was directly correlated with the relative wetted area.

3.3. Effect of the Relative Diameter of the Balsa Wood on the Bio-DFADs

To examine whether the diameter of the balsa wood affected the hydrodynamic performance of the Bio-DFADs, six diameters of the balsa wood (0.03, 0.04, 0.05, 0.06, 0.07, and 0.08 m) were selected and applied, for $\alpha = 0°$, L_F = 0.50 m, and U = 0.50 m/s, as depicted in Figure 12.

Figure 12a illustrates the relationship between the relative velocity, V/U, and the relative diameter, D_F/B, of the Bio-DFADs. The enlargement of the diameter initially led to a significant decrease in relative velocity, with a diminishing inclination to drop as the diameter increased. According to Figure 12b, the ratio of the wetted area to the total area, S_{Wetted}/S_{Total}, decreased considerably and subsequently reached a stable state as the diameter increased. Figure 12c illustrates the correlation between the relative diameter and the relative tension, F/W_{Sinker}. As the diameter of the object increased, the tension slightly decreased. As the relative diameter increase, the buoyancy of the Bio-DFADs became greater than the gravity, then the more surface of the model out the water, and lead to the

decrease of the relative wetted area. Due to the decrease of the relative wetted area, the fluid force acting on the model decreases, and then leads to a decline of the relative velocity. The findings indicated that the size of the balsa wood had a notable impact on the velocity and the surface area in contact with water while having minimal effect on the rope tension. The correlation between the relative velocity and the wetted surface area agrees with the results presented in the previous section.
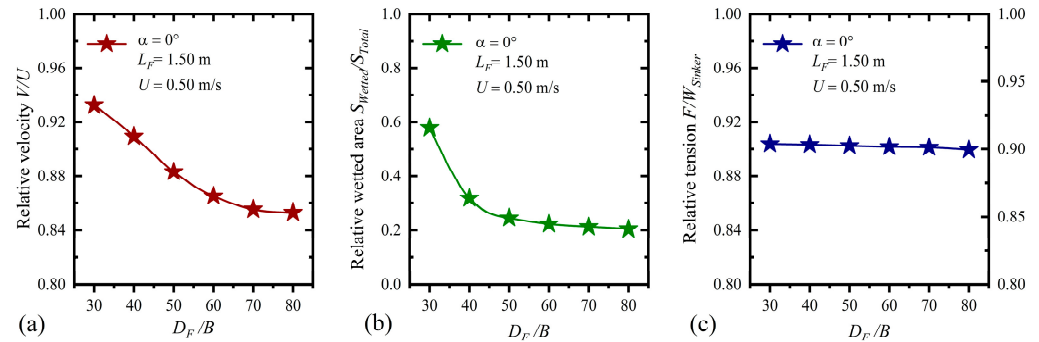
Figure 12. The change in (**a**) relative velocity (V/B), (**b**) wetted area (S_{Wetted}/S_{Total}), and (**c**) rope tension (F/W_{Sinker}) of the Bio-DFADs for different balsa wood diameters.

3.4. Effect of the Relative Weight of the Sinker on the Bio-DFADs

To investigate whether the relative weight of the sinker affected the hydrodynamic performance of the Bio-DFADs, seven sinker weights (2.00, 4.00, 6.00, 8.00, 10.00, 12.00, and 14.00 kg) were selected and applied, for $\alpha = 0°$, $L_F = 0.50$ m, and $U = 0.50$ m/s, as depicted in Figure 13.
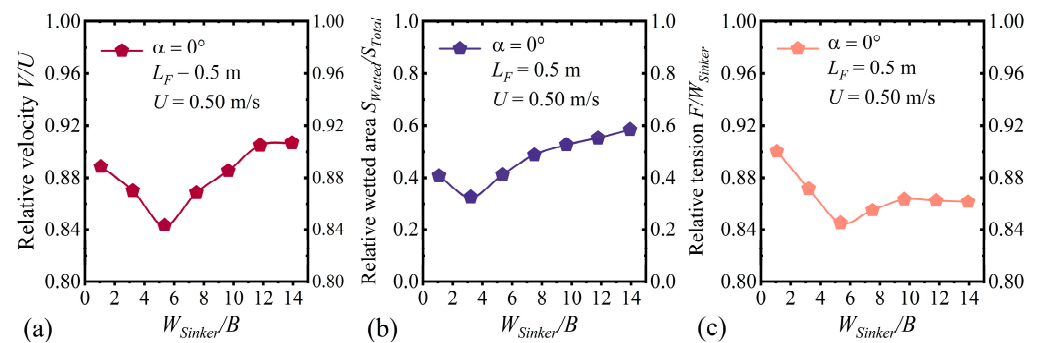
Figure 13. The change in (**a**) relative velocity (V/U), (**b**) wetted area (S_{Wetted}/S_{Total}), and (**c**) rope tension (F/W_{Sinker}) of the Bio-DFADs for different sinker weights.

Figure 13a demonstrates the relationship between the relative velocity, V/U, and the relative weight of the sinker, W_{Sinker}/B. The relative velocity initially decreased and then increased as the relative weight increased. The relative velocity reached a minimum when W_{Sinker}/B was 6. According to Figure 13b, the wetted area also decreased and then increased as the relative weight increased, and the wetted area reached a minimum when W_{Sinker}/B was 4. According to Figure 13c, the relative tension followed a similar trend, initially decreasing and then increasing as the relative weight increased, and the relative tension reached its lowest point when W_{Sinker}/B was 6. Therefore, the weight of the sinker had a notable impact on the hydrodynamic performance of the Bio-DFADs. As the relative weight increase, a minimum value occurs in the relative velocity, relative wetted area, and relative tension, but at different relative weight value. The phenomenon can be explained by the fact that as the weight of the sinker increases, due to the gravity being greater than the fluid force acting on the sinker, the angle between the sinker and rope decreases, then leads to more surface of the raft out the water. Hence, the wetted area declines and the fluid force acting on the Bio-DFADs decreases and leads to the decrease of relative velocity. However, as the weight continues to rise, the fluid force becomes great than the gravity

of sinker, then the angle between the sinker and rope increases, and leads to the relative velocity, relative wetted area, and relative tension increasing. The Bio-DFADs can remain in the fishing area for a predetermined duration while maintaining a reduced speed, but notably, the relative velocity only experiences a drop within a specific range of W_{Sinker}/B.

4. Conclusions

This study investigates the hydrodynamic performance of Bio-DFADs in a pure current using CFD simulations. The effects of the relative current velocity, attack angle, relative diameter of the balsa wood, and relative weight of the sinker on the relative velocity, wetted surface, and rope tension were examined. The key conclusions can be summarized as follows:

(1) The relative current velocity had a substantial impact on the relative velocity. However, the differences in relative velocity among the three models was modest. Additionally, the relative current velocity had a negligible influence on the relative wetted area and the rope tension.

(2) The relative length exerted a substantial impact on the relative velocity and the relative wetted area in pure current while having a minimal influence on the relative tension. The hydrodynamic performance of the model was minimally affected by the attack angle. There was a direct correlation between the relative velocity and the relative wetted area.

(3) The diameter of the balsa wood had a notable impact on the velocity and wetted area but had a minimal effect on the rope tension.

(4) The sinker's relative weight had a notable impact on the hydrodynamic performance of the Bio-DFADs. The Bio-DFADs can remain in the fishing area for a predetermined duration while moving at a reduced speed. However, the relative velocity was only diminished within a specific range of relative weight of sinker.

This study investigates the hydrodynamic characteristics of the Bio-DFADs, aiming to explore structural forms that combine low drift velocities with biodegradability. The goal is to maximize the retention of fish aggregating devices within the fishing grounds during operations of tuna purse-seine fleets. Additionally, even in cases of damage or sinking, the study aims to minimize marine environmental pollution by employing biodegradable materials.

The present investigation focused on the hydrodynamic performance in undiluted current conditions. Further investigation is required to examine the impact of waves on the hydrodynamic characteristics of various Bio-DFAD geometries. The wave mainly influences the motion responses of the raft and the rope tension. Hence, the wave may have an important influence on the relative velocity, relative rope tension, and relative wetted area. Furthermore, it is necessary to investigate the impact of wave-current interactions on the Bio-DFADs in future research.

Institutional Review Board Statement: Not applicable.

Informed Consent Statement: Not applicable.

Data Availability Statement: Data are contained within the article and are available from the corresponding author upon reasonable request.

References

1. ISSF. *Status of the World Fisheries for Tuna*; ISSF Technical Report 2022-04; International Seafood Sustainability Foundation: Washington, DC, USA, 2022.
2. Maufroy, A.; Chassot, E.; Joo, R.; Kaplan, D.M. Large-scale examination of spatio-temporal patterns of drifting fish aggregating devices (dFADs) from tropical tuna fisheries of the Indian and Atlantic Oceans. *PLoS ONE* **2015**, *10*, e0128023. [CrossRef] [PubMed]
3. Imzilen, T.; Lett, C.; Chassot, E.; Kaplan, D.M. Spatial management can significantly reduce dFAD beachings in Indian and Atlantic Ocean tropical tuna purse seine fisheries. *Biol. Conserv.* **2021**, *254*, 108939. [CrossRef]
4. Escalle, L.; Hare, S.R.; Vidal, T.; Brownjohn, M.; Hamer, P.; Pilling, G. Quantifying drifting Fish Aggregating Device use by the world's largest tuna fishery. *ICES J. Mar. Sci.* **2021**, *78*, 2432–2447. [CrossRef]
5. Lopez, J.; Roman, M.H.; Lennert-Cody, C.; Maunder, M.N.; Vogel, N. Floating object fishery indicators: A 2020 report. In Proceedings of the IATTC-5th Meeting of the Ad Hoc Working Group on FADs, San Diego, CA, USA, 6 May 2021.
6. Evans, K.; Young, J.; Nicol, S.; Kolody, D.; Allain, V.; Bell, J.; Brown, J.; Ganachaud, A.; Hobday, A.; Hunt, B.; et al. Optimising fisheries management in relation to tuna catches in the western central Pacific Ocean: A review of research priorities and opportunities. *Mar. Policy* **2015**, *59*, 94–104. [CrossRef]
7. Maufroy, A.; Kaplan, D.M.; Bez, N.; De Molina, A.D.; Murua, H.; Floch, L.; Chassot, E. Massive increase in the use of drifting Fish Aggregating Devices (dFADs) by tropical tuna purse seine fisheries in the Atlantic and Indian oceans. *ICES J. Mar. Sci.* **2017**, *74*, 215–225. [CrossRef]
8. Wain, G.; Guery, L.; Kaplan, D.M.; Gaertner, D. Quantifying the increase in fishing efficiency due to the use of drifting FADs equipped with echosounders in tropical tuna purse seine fisheries. *ICES J. Mar. Sci.* **2021**, *78*, 235–245. [CrossRef]
9. Dupaix, A.; Capello, M.; Lett, C.; Andrello, M.; Barrier, N.; Viennois, G.; Dagorn, L. Surface habitat modification through industrial tuna fishery practices. *ICES J. Mar. Sci.* **2021**, *78*, 3075–3088. [CrossRef]
10. Marsac, F.; Fonteneau, A.; Ménard, F. Drifting FADs used in tuna fisheries: An ecological trap? In Proceedings of the Pêche thonière et dispositifs de concentration de poissons, Caribbean-Martinique, France, 15–19 October 1999.
11. Itano, D.; Fukofuka, S.; Brogan, D. The development, design, and current status of anchored and drifting FADs in the WCP. In Proceedings of the 17th Meeting of the Standing Committee on Tuna and Billfish, Majuro, Marshall Islands, 9–18 August 2004; p. 26.
12. Hallier, J.P.; Gaertner, D. Drifting fish aggregation devices could act as an ecological trap for tropical tuna species. *Mar. Ecol. Prog. Ser.* **2008**, *353*, 255–264. [CrossRef]
13. Dagorn, L.; Holland, K.N.; Restrepo, V.; Moreno, G. Is it good or bad to fish with FADs? what are the real impacts of the use of drifting FADs on pelagic marine ecosystems? *Fish Fish.* **2012**, *14*, 391–415. [CrossRef]
14. Moreno, G.; Salvador, J.; Zudaire, I.; Murua, J.; Pelegrí, J.L.; Uranga, J.; Murua, H.; Grande, M.; Santiago, J.; Restrepo, V. The jelly-FAD: A paradigm shift in the design of biodegradable fish aggregating devices. *Mar. Policy* **2022**, *174*, 105352. [CrossRef]
15. Murua, H.; Zudaire, I.; Tolotti, M.; Murua, J.; Capello, M.; Basurko, O.C.; Krug, I.; Grande, M.; Arregui, I.; Uranga, J.; et al. Lessons learnt from the first large-scale biodegradable FAD research experiment to mitigate drifting FADs impacts on the ecosystem. *Mar. Policy* **2023**, *148*, 105394. [CrossRef]
16. Moreno, G.; Salvador, J.; Murua, J.; Phillip, N.B., Jr.; Murua, H.; Escalle, L.; Zudaire, I.; Pilling, G.; Restrepo, V. *A Multidisciplinary Approach to Build New Designs of Biodegradable Fish Aggregating Devices (FADs)*; WCPFC Sci. Comm. WCPFC-SC16-2020/EB-IP-XX; WCPFC: Washington, DC, USA, 2020.
17. Wang, Y.; Zhou, C.; Xu, L.; Wan, R.; Shi, J.; Wang, X.; Tang, H.; Wang, L.; Yu, W.; Wang, K. Degradability evaluation for natural material fibre used on fish aggregation devices (FADs) in tuna purse seine fishery. *Aquac. Fish.* **2021**, *6*, 376–381. [CrossRef]
18. Zhang, T.; Liu, Z.; Zhang, J.; Su, X.; Chen, J.; Wan, R. Numerical Study of the Hydrodynamic Response of Biodegradable Drifting Fish Aggregating Devices in Regular Waves. *Fishes* **2024**, *9*, 112. [CrossRef]
19. Zhou, Y.; Zhang, X.; Chen, J.; Liu, R.; Sun, J.; Si, Y. Catenary Mooring Length Control for Motion Mitigation of Semi-Submersible Floating Wind Turbines. *J. Mar. Sci. Eng.* **2024**, *12*, 628. [CrossRef]
20. Cutajar, C.; Sant, T.; Farrugia, R.N.; Buhagiar, D. Analysis of the Wave Attenuating and Dynamic Behaviour of a Floating Breakwater Integrating a Hydro-Pneumatic Energy Storage System. *J. Mar. Sci. Eng.* **2023**, *11*, 2189. [CrossRef]
21. Wang, S.; Liu, S.; Xiang, C.; Li, M.; Yang, Z.; Huang, B. Prediction of Wave Forces on the Box-Girder Superstructure of the Offshore Bridge with the Influence of Floating Breakwater. *J. Mar. Sci. Eng.* **2023**, *11*, 1326. [CrossRef]
22. Yuan, Y.; Xue, H.; Tang, W. Internal laminar flow effect on the nonlinear dynamic response of marine risers under uniform ocean current. *Ships Offshore Struct.* **2022**, *17*, 1382–1391. [CrossRef]
23. Zhao, Y.P.; Bai, X.D.; Dong, G.H.; Bi, C.W. Deformation and stress distribution of floating collar of net cage in steady current. *Ships Offshore Struct.* **2019**, *14*, 371–383. [CrossRef]

24. Zhang, Y.; Feng, L.; Zhang, L.; Wang, L.; Dong, S.; Gao, Q.; Hu, X.; Li, J. A study of tension and deformation of flexible net under the action of current. *Ships Offshore Struct.* **2022**, *19*, 27–44. [CrossRef]

25. González, M.; Karumathil, S.K. A new method to estimate the resistance coefficients of net panels modeled as porous media. *Ocean Eng.* **2023**, *274*, 113952. [CrossRef]

26. Wan, R.; Zhang, T.; Zhou, C.; Zhao, F.; Wang, W. Experimental and numerical investigations of hydrodynamic response of biodegradable drifting Fish Aggregating Devices (FADs) in waves. *Ocean Eng.* **2022**, *244*, 110436. [CrossRef]

27. Xiao, Y.; Zhou, C.; Zhang, T.; Wang, Y.; Xie, C.; Zhang, Y. Aggregation characteristics of fish aggregating devices (FADs) in tuna purse seine fisheries in the Western and Central Pacific Ocean. *J. Fish. China* **2023**, *47*, 039719.

28. Lee, K.; Lee, S.I.; Kim, D.N. Fluid Dynamics Analysis of Fish Aggregation Device using Particle Image Velocimetry. In Proceedings of the IOTC-2018-WPTT20-24, the 20th Session of the IOTC Working Party on Tropical Tunas, Mahé, Seychelles, 29 October–3 November 2018.

29. Shih, T.H.; Liou, W.W.; Shabbi, A.; Yang, Z.; Zhu, J. A new k-ε eddy-viscosity model for high Reynolds number turbulent flows—Model development and validation. *Comput. Fluids* **1995**, *24*, 227–238. [CrossRef]

30. Fuhrman, D.R.; Li, Y. Instability of the realizable k-ε turbulence model beneath surface waves. *Phys. Fluids* **2020**, *32*, 115108. [CrossRef]

31. Hirt, C.W.; Nichols, B.D. Volume of fluid (VOF) method for the dynamics of free boundaries. *J. Comput. Phys.* **1981**, *39*, 201–225. [CrossRef]

32. Lin, P.; Liu, P.L.F. A Numerical Study of Breaking Waves in the Surf Zone. *J. Fluid Mech.* **1998**, *359*, 239–264. [CrossRef]

33. Rodi, W. *Turbulence Models and Their Application in Hydraulics—A State of the Art Review*; IAHR Monograph: Delft, The Netherlands, 1980.

34. *STAR-CCM+ User's Guide*; Siemens PLM Software: Plano, TX, USA, 2019.

35. Choi, J.; Yoon, S.B. Numerical simulations using momentum source wave-maker applied to RANS equation model. *Coast. Eng.* **2009**, *56*, 1043–1060. [CrossRef]

36. Gu, H.; Stansby, P.; Stallard, T.; Carpintero Moreno, E. Drag, added mass and radiation damping of oscillating vertical cylindrical bodies in heave and surge in still water. *J. Fluids Struct.* **2018**, *82*, 343–356. [CrossRef]